Integral Field Spectroscopy of Compact Elliptical Galaxies.

Kristopher Andrew Clark

A thesis submitted in partial fulfilment
of the requirements for the degree of
Master of Science

Jeremiah Horrocks Institute for Mathematics, Physics and Astronomy
University of Central Lancashire

March 2020

Declaration

Type of Award: Master of Science

School: Physical Sciences and Computing

I declare that while registered as a candidate for the research degree, I have not been a registered candidate or enrolled student for another award of the University or other academic or professional institution.

I declare that no material contained in the thesis has been used in any other submission for an academic award and is solely my own work.

No proof-reading service was used in the compilation of this thesis.

Kristopher Andrew Clark

March 2020

Abstract

The rare compact elliptical galaxies (cEs) are thought to have been formed through a tidal stripping process of a once much larger progenitor, as they do not adhere to the mass-size, mass-metalicity and black hole-bulge mass scaling relations like their more massive early-type cousins. By using observations taken with the FLAMES/GIRAFFE integral field spectrographs of the European Southern Observatory's (ESO) 8.2m Very Large Telescope (VLT), we searched for evidence for the presence of overly massive SMBHs in our sample of cEs. The raw reduction was performed by the workflow environment EsoReflex, Voronoi binned spectra from 4 target cEs were obtained using the VorBin method. We performed a full spectrum fit of cE spectra using the Penalized Pixel Fitting (pPXF) method, to extract resolved kinematics i.e the Line Of Sight Velocity Distribution (LOSVD). Dynamical mass estimates of order $10^9 M_\odot$ were obtained. Dynamical to stellar mass ratios for 3 cEs (NGC5846cE, NGC3268cE1 and AHcE0) reveal the likely presence of an overly massive SMBH, favoring the tidal stripping scenario for cE formation.

Contents

Acknowledgements

I would like to thank Mark Norris for all of his hard work guiding me through this project. Without his world class expertise and guidance this work would not have been possible. I would also like to thank David Glass, Tom Davidson and Jordan Thirlwall for their advice on several occasions. A huge thank you must be given to Jenny, for the moral support and motivation throughout the project.

List of Figures

CHAPTER 0

List of Tables

Chapter 1

Introduction

1.1 Compact Elliptical Galaxies

Compact elliptical galaxies (cEs) are a relatively rare class of Compact Stellar System (CSS) with only ~ 200 currently known (Ferré-Mateu et al., 2018; Norris et al., 2014). They are characterised by their intermediate luminosity, high surface brightness with correspondingly high stellar densities (see Figure 1.1) and compact nature with effective radii R_e, (i.e the radii at which half the light of the galaxy is emitted) ranging between $0.1kpc \leq R_e \leq 1kpc$, and dynamical masses of the order $10^9 M_\odot$ (Ferré-Mateu et al., 2018). The number of known cEs and other CSS such as Ultra Compact Dwarfs (UCD), Dwarf Elliptical (dE) and Dwarf spheroidal (dSph) has markedly increased since the AIMSS (Archive of Intermediate Mass Stellar Systems) project (Janz et al., 2016; Norris et al., 2014). This project has essentially filled the gap between two previously distinct stellar systems, Globular Clusters (GCs) and Elliptical galaxies (Es). The presence of cEs in this intermediate space between GCs and early-type galaxies leads naturally to the question of their physical nature and the processes in which they form. The archetypal, first to be discovered and perhaps the best studied cE is M32. M32 has been found to have several stellar populations with $\sim$ 40 % of stars between 2-5 Gyr and 55 % of stars older than 5 Gyr with

a mass-weighted age and metallicity of $\langle age \rangle \sim$ 6.8Gyr and $\langle M/H \rangle$ = -0.01 dex respectively (Monachesi et al., 2012). Therefore M32 is relatively old and as metal-rich as larger galaxies with the addition of the stellar populations of different age, which implies a complex formation history. M32 is bound to M31, the Andromeda galaxy and like M32, cEs are typically found orbiting or in proximity to larger "host" galaxies (Ferré-Mateu et al., 2018) and galaxy cluster environments(Infante et al., 2003; Martinović & Micic, 2017). Several suggestions have been proposed to explain the mechanisms that lead to cE formation, each is described in turn below.

Figure 1.1: The archetypal cE M32. The background structure in this image is M31:the Andromeda galaxy. From this the compact nature of M32 can be seen. Credit:(universetoday.com)

1.1.1 Formation by Tidal Stripping

It is widely believed that the most likely scenario in which cEs form is the tidal stripping of a once much more massive progenitor (Chilingarian & Bergond, 2010; Norris et al., 2014), most likely lenticular or spiral galaxies (Chilingarian et al., 2008). The gravity of the larger host galaxy removes the dark matter halo and subsequently the outer more loosely-bound stars, leaving the tightly bound self-gravitating bulge of the smaller galaxy behind. Supporting this is the "smoking gun" evidence of tidal interactions between some cEs and their host galaxy, with clear tidal streams of stars being removed from the cE by a much larger host galaxy (Huxor et al., 2011) and the radial surface brightness profile of M32 perfectly resembling a bulge with a small residual disk component (Graham, 2002).

In addition cEs are outliers on the scaling relations that their much more massive cousins the early-type galaxies adhere to, such as the mass-size, Black Hole (BH) bulge-mass (Häring & Rix, 2004; van den Bosch, 2016) and mass-metallicity, (see Janz et al. 2016). They are outliers of the mass-size BH scaling relation because for the mass and size of cEs, the BHs are too massive. The BH mass in the tidal stripping scenario would remain essentially unchanged as the mass of the galaxy decreased through the loss of stars. If cEs do not follow these well established relationships then having an overly massive black hole indicates that cEs were once much larger in past epochs and harbour an overly massive BH as a result.

cEs are also outliers on the mass-metallicity scaling relation, this is because they are too metal rich, being as metal-rich as the centres of larger galaxies. The enhanced metallicity [M/H], is because only the inner most metal-rich part of the stripped galaxy remains in this scenario. More massive galaxies tend to be more metal-rich because they can retain heavy elements from SuperNovae (SN) ejecta due to their deeper gravitational field, however, cEs are relatively low mass hence should not be so rich in metals. Furthermore, while cEs are more compact and denser than

typical ellipticals and lenticulars, they actually resemble the central regions of such galaxies in terms of these properties.

Although cEs are mostly found orbiting a host galaxy, a small number of them have been found isolated in the field, with the nearest likely host being $\sim$ 900 kpc away (Huxor et al., 2013). These isolated cEs are conjectured to have been ejected from a galaxy group or cluster via a three-body interaction, which leads the much smaller cE to be ejected when two larger galaxies interact (Chilingarian et al., 2009). The three-body interaction is one explanation for the isolated cEs, however an understanding of the prevalence of isolated cEs is needed to solve this issue as the conditions leading to ejection via three-body interactions are likely to be rare. The existence of a large population of isolated cEs may indicate other mechanisms may be at work in forming cEs. Other alternative formation scenarios will now be discussed.

1.1.2 Formation by gas-rich starburst

There exists a population of Elliptical galaxies at high redshift (z = 2) resembling the larger analogues of today's dwarf galaxies, therefore cEs (Yıldırım et al., 2017), leading to speculation that cEs could form in the same manner. Because cEs could be low mass extensions in the early-type galaxy sequence(Ferré-Mateu et al., 2018; Wirth & Gallagher, 1984), therefore they could form in the same manner as early-types i.e through gas-rich starburst. In this scenario the early period of early-type galaxy growth is through successive wet mergers of smaller galaxies to create larger ones, i.e gas rich galaxies merging together. The merger through tidal interactions causes the now surplus gas to collapse and form new stars at an accelerated rate (Kormendy et al., 2009). In this situation it would be expected that the BHs would be appropriate for the size of the galaxy according to the scaling relations and therefore the black holes should not be overly massive. The metallicity would also

generally be expected to follow the mass-metallicity relation and the resulting cE would not be expected to be denser than typical early-type galaxies.

1.1.3 Formation by ram pressure confinement

A further hypothesis for cE formation is by ram pressure confinement. The work of Du et al. 2018 produced cE like objects in their simulations using a mechanism they call ram pressure confinement. Ram pressure confinement is where a galaxy's gas is forced into the bulge or central regions due to a pressure exerted as it moves through the intra-cluster medium at great speed. This then triggers a major star forming event which rapidly builds up the stellar density in the central regions. In addition the ram pressure also confines SN ejecta, this leads to a rapid increase in metallicity which explains why cEs do not follow the mass-metallicity scaling relation. It is unclear in this scenario whether the BH could be overly massive. If the BH is fed mass at the same time as the starburst it is possible stellar mass and BH mass could grow in sync, however more simulations are required to investigate this.

Now we have explored the proposed formation mechanisms of cEs and the likely mass of BHs in each situation, we will now outline the aims of this work and the logistics of investigating such questions.

1.2 Aims of the project

The aim of this work is to extract kinematic measurements for a sample of cEs to search for evidence of the presence of Super Massive Black Holes (SMBHs), using spectroscopic observations taken with the FLAMES/GIRAFFE spectrograph of UT2 (Kueyen) of the Very Large Telescope (VLT). This is done by extracting spatially resolved kinematics i.e. the line of sight velocity distribution (LOSVD),

particularly the central velocity dispersion. The velocity dispersion (the mean dispersion/distribution about the line of sight velocity) contains information about the gravitational potential, hence the influence on the mass in the potential. A large dispersion implies a large mass is exerting its influence on the orbits of stars in the pressure supported system. The central velocity dispersion will then be used to find a dynamical mass M_{dyn} estimate of the cEs assuming the central regions contain negligible amounts of dark matter and gas. Then by using literature values for stellar mass, a dynamical mass to stellar mass ratio (M_{dyn}/M_*) can be plotted. Any cEs above the 1:1 or unity line in these plots could indicate the presence of an overly massive SMBH. Black holes and galaxy mass are thought to grow in tandem, that is to say black holes and galaxies scale together, so if evidence of an overly massive SMBH is found (as in previous studies) the tidal stripping scenario gains support. If evidence of our cEs being host to a SMBH is found, then confirmation will be subsequently sought with follow-up observations using high spatial resolution Adaptive Optics (AO) in order to confirm the BH mass.

This thesis is organised as follows. In the remaining sections of Chapter 1 our target cEs will be discussed. Chapter 2 describes the multiple stages of the reduction of our observational data; the removal of cosmic rays, the basic data reduction, sky subtraction and the Voronoi binning of the resulting spectra. Chapter 3 will focus on the acquisition of measurements from our data via a full spectrum fit using the penalised pixel fitting method (pPXF). In Chapter 4 we present the results of the full spectrum fits and in Chapter 5 we will discuss the implications of the results and the outlook continuation of this work.

1.2.1 Properties of observations

Integral Field Spectroscopy (IFS) was conceptualised in 1982 (Courtes, 1982) and the subsequent first use of an integral field unit (IFU) was in 1987 with the TIGER

IFU of Canada-France-Hawaii Telescope (CFHT). Even in the pioneering days IFS was found to be "far superior to long-slit spectrography for high resolution purposues" (Bacon et al., 1995). Since the pioneering days IFUs have become ubiquitous, with most of the worlds largest telescopes having IFS capabilities. The long exposure times needed to observe faint extended objects is time consuming, using traditional long-slit spectroscopy would therefore take many hours to obtain 2-D spatial coverage of an extended object. With IFS, spectra from distinct regions across the target galaxy can obtained in one observation, which considerably reduces the required telescope time. This is possible due to the main characteristic difference between IFS and classical spectroscopic methods. With IFS the light collected is kept separated by glass fibre optic bundles, or by dividing it up by means of small mirrors in the case of the image slicer type. The light from different regions is kept separate so 2-D spatial information is preserved.

There are several different designs and variants of IFU, these include; The micro-lens array, image slicer and fibre bundles. The image slicer method slices a 2-D image into strips and each strip is placed in front of a slit and then through the dispersive element (Vivès & Prieto, 2005), UVES is one example of this type (Dekker et al., 2000). The fibre bundle variant is where light enters glass fibre optic bundles placed in the focal plane and exits the fibres through the slit. An example of this type includes the SDSS IFU, MaNGA (Bundy et al., 2015). The micro-lens array or lenslet array is where an array of micro lenses is placed in the plane of the spectrograph fibres, the light then is passed through the array lenses and through the dispersive element on to a CCD, such as the IFU of SINFONI (Eisenhauer et al., 2003). In this work the instrument we used is of the micro-lens array type.

The Integral Field Spectroscopy (IFS) data used for this work was collected in service mode for Dr M.Norris in 2014 at ESO's VLT UT2 at the Paranal observatory Chile. Note: Adaptive optics was unavailable at the time of observation. The

VLT UT2 houses the the FLAMES fiber facility, which feeds two spectrographs, UVES and GIRAFFE (Pasquini et al., 2002) The GIRAFFE spectrograph has several observation modes, these include the multi-fibre mode Medusa which allows for observations of up to 132 separate objects, IFU and ARGUS mode. For this work ARGUS mode was used and as mentioned this is a micro-lens array. In this mode only one object can be observed at any one time. It consists of a 14×22 micro-lens array, each lens is 0.2×0.2 arc seconds per pixel. The wavelength range used for our observations was in the Near Infra-Red (NIR), the wavelength coverage between 8182 and 9377Å. This wavelength range covers the CaII absorption triplet, which is a prominent absorption feature that can be used to perform a full spectrum fit to extract kinematic information from our targets. The CaII triplet is the only strong absorption feature in our wavelength range and is relatively free from contamination from any neighbouring absorption features such as the weak FeI absorption features. The three emission lines of the CaII triplet have rest wavelengths at 8498, 8542 and 8662Å.

1.2.2 Observational Sample

Our sample of seven cEs are a subset of a larger sample chosen to cover a range of mass, density and environment displayed by cEs (see Table 1.1). Unfortunately the full sample was not observed so coverage of certain parameters is limited. Of our sample five cEs are found in galaxy clusters (Abell496, Abell400, NGC3268cE1, ESO133005 and NGC4696cE), 2 have been previously well studied (NGC5846cE and NGC3268cE1), our sample also includes AHcE0 which is one of the isolated cEs from Huxor et al. 2013. One of our cEs has no previous velocity dispersion information published (NGC4696cE) and in general the remaining sample have only single integrated velocity dispersion measures. Unfortunately the small sample size is heavily biased towards cEs in cluster environments, which limits our ability to

probe the role of environment on cE formation. However by comparison of our measurements of our well studied cEs with literature values we can assess whether the measurements of NGC4696cE are reliable.

Object	RA	Dec	Redshift(z)	Environment	Exp time(s)
NGC5846cE	15:06:34	01:33:30	0.0057	Group	2 x 2775
NGC3268cE1	10:30:04	-35:20:32	0.0093	Cluster	4 x 2775
NGC4696cE	12:48:53	-41:19:05	0.0073	Cluster	2 x 2775
AHcE0	09:47:29	14:12:44	0.0198	Isolated	3 x 2775
Abell400cE	02:57:44	06:02:01	0.0254	Cluster	3 x 2775
Abell496cE	04:33:37	-13:15:19	0.0329	Cluster	4 x 2775
ESO133005	13:30:05	-20:55:21	0.0180	Cluster	7 x 2775

Table 1.1: The basic properties of our observational sample of cEs. In the table the positions of our targets in RA and Dec (J2000.0 equinox) along with the red-shifts, environment and total exposure times are given.

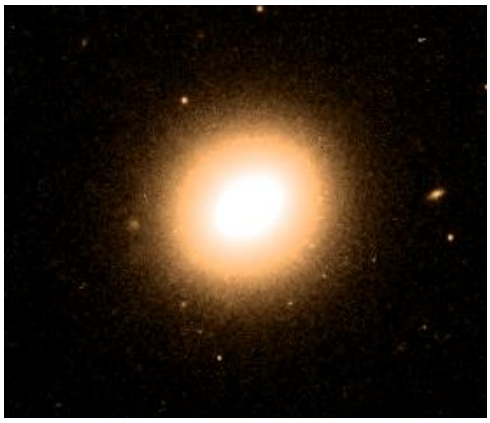

(a) Hubble space telescope image of NGC5846cE

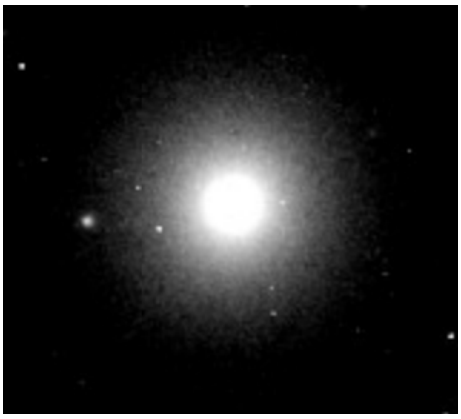

(b) Hubble image of NGC3268cE1

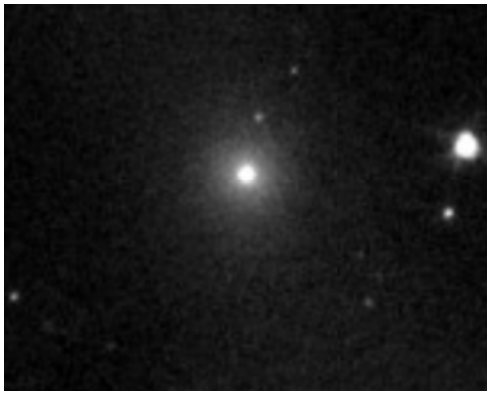

(c) ESO13cE

(d) NGC4696cE

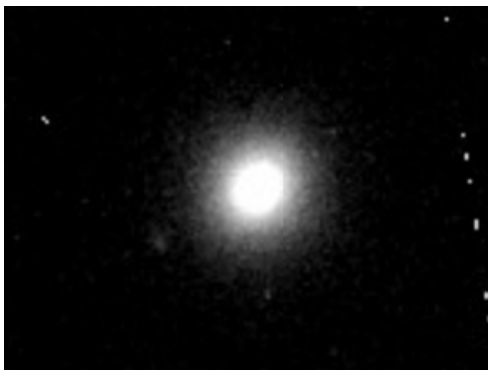

(e) Abell400cE

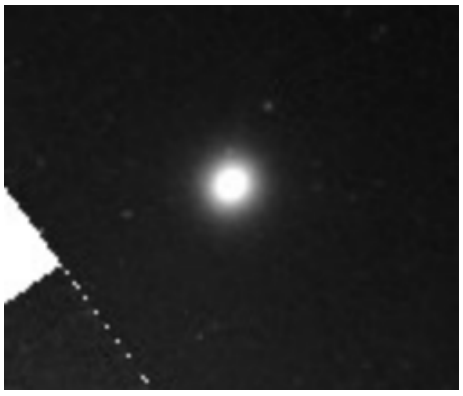

(f) Abell496cE

Figure 1.2: The images above are Hubble legacy archive images of our sample of cEs. These images are a combination of several images at different wavelengths to produce colour images of the cEs. The absolute magnitudes for the targets are between -12 and -18 mag

Chapter 2

Data Reduction

The raw science data collected for this work requires several steps of reduction before it is suitable for analysis. These steps were; the cleaning of cosmic rays with the Laplacian cosmic ray detection algorithm LA cosmic (van Dokkum, 2001), the use of ESO's reduction pipeline software EsoReflex to perform the basic data reduction and construct a data cube (Freudling et al., 2013), a subtraction of the sky emission lines and background galaxy light (sky subtraction). Then the VorBin method (Cappellari & Copin, 2003) was used to bin adjacent spaxels to a constant minimum signal to noise ratio (SNR). These reduction steps will now be described in more detail.

2.1 Cosmic Ray Cleaning

The first step in the reduction of the raw data is cosmic ray cleaning. Cosmic rays are high energy particles that hit the CCD during telescope observations. It is necessary to clean cosmic ray hits from the main science frame before it is included in the set of files to be used with EsoReflex, this is because cosmic rays complicate subsequent reduction, especially the sky subtraction as they lead to inaccurate fits to the background. The cosmic ray cleaning was implemented with python using

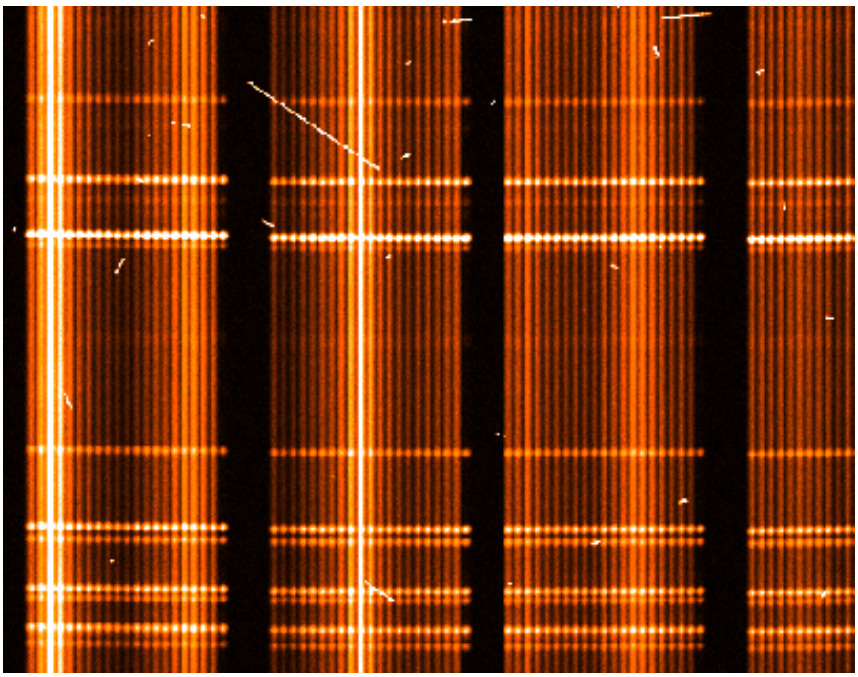

Figure 2.1: Raw science frame before the application of LA cosmic. The cosmic ray hits are clearly visible as bright streaks, some span several fibres.

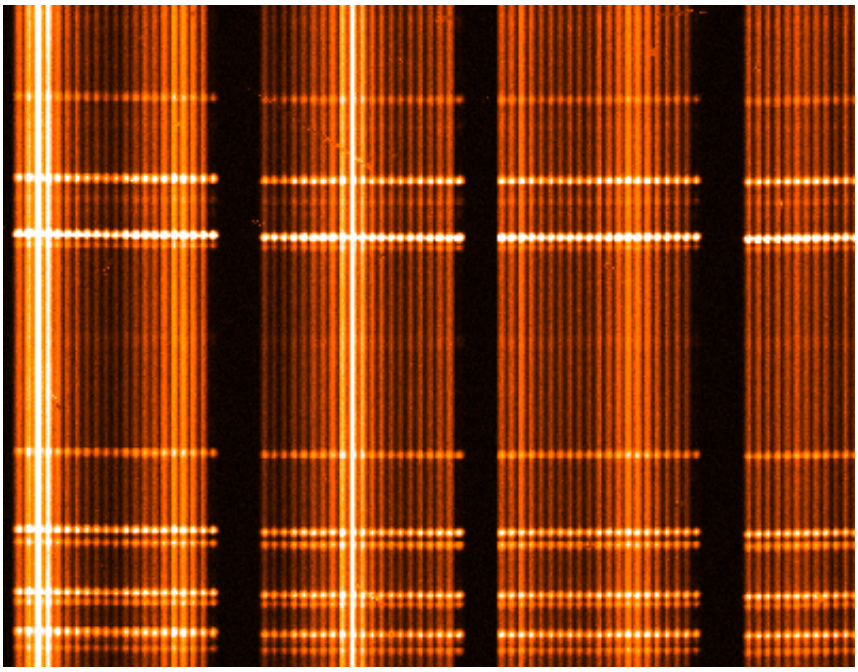

Figure 2.2: The Figure shows the science frame post cosmic ray cleaning. The obvious streaks from 2.1 have been removed or significantly reduced.

the LA Cosmic algorithm of van Dokkum 2001. LA Cosmic is able to detect cosmic ray hits on the CCD because they have a sharp edge compared to smooth point spread function as displayed by data that has passed through the telescope and instrument optics. In Figures 2.1 and 2.2 an example of a raw science frame is seen before and after cleaning with LA cosmic, the white streaks in the science frame before cleaning have been removed/reduced in the following image (after the use of LA Cosmic). The Figures show a subsection of the whole frame. In these images wavelength is on vertical axis, 4 out of the 14 Y-dimension pixels can be seen as distinct blocks separated by the sub-slits (blank black spaces running vertically) and the 22 X-dimension pixels are seen in each block as 22 lines running vertically. The bright regions in the images are the sky emission lines, that are to be removed in the reduction process. The dark regions are absorption features.

2.2 EsoReflex

The IFU spectrographs at the VLT such as FLAMES/GIRAFFE, MUSE etc require complex multi-step data reduction processes. As a consequence the reduction of IFU data has a deserved reputation for being time-consuming compared to traditional astronomical observations, this is because of the large number of raw calibration files and a correspondingly large number of steps in the reduction of the raw data. This increases the chance of basic accounting errors, such as forgetting a frame in the creation of the master bias. In an attempt to minimise errors and cut down on reduction time ESO have developed their own data reduction pipeline software package, which is available for all of the IFUs at ESO's telescopes. This software is called EsoReflex or simply Reflex [1].

Reflex is a data reduction work-flow built on the Kepler work-flow platform (Freudling et al., 2013). Reflex performs the reduction using a "director" and a

[1] `https://www.eso.org/sci/software/esoreflex/`

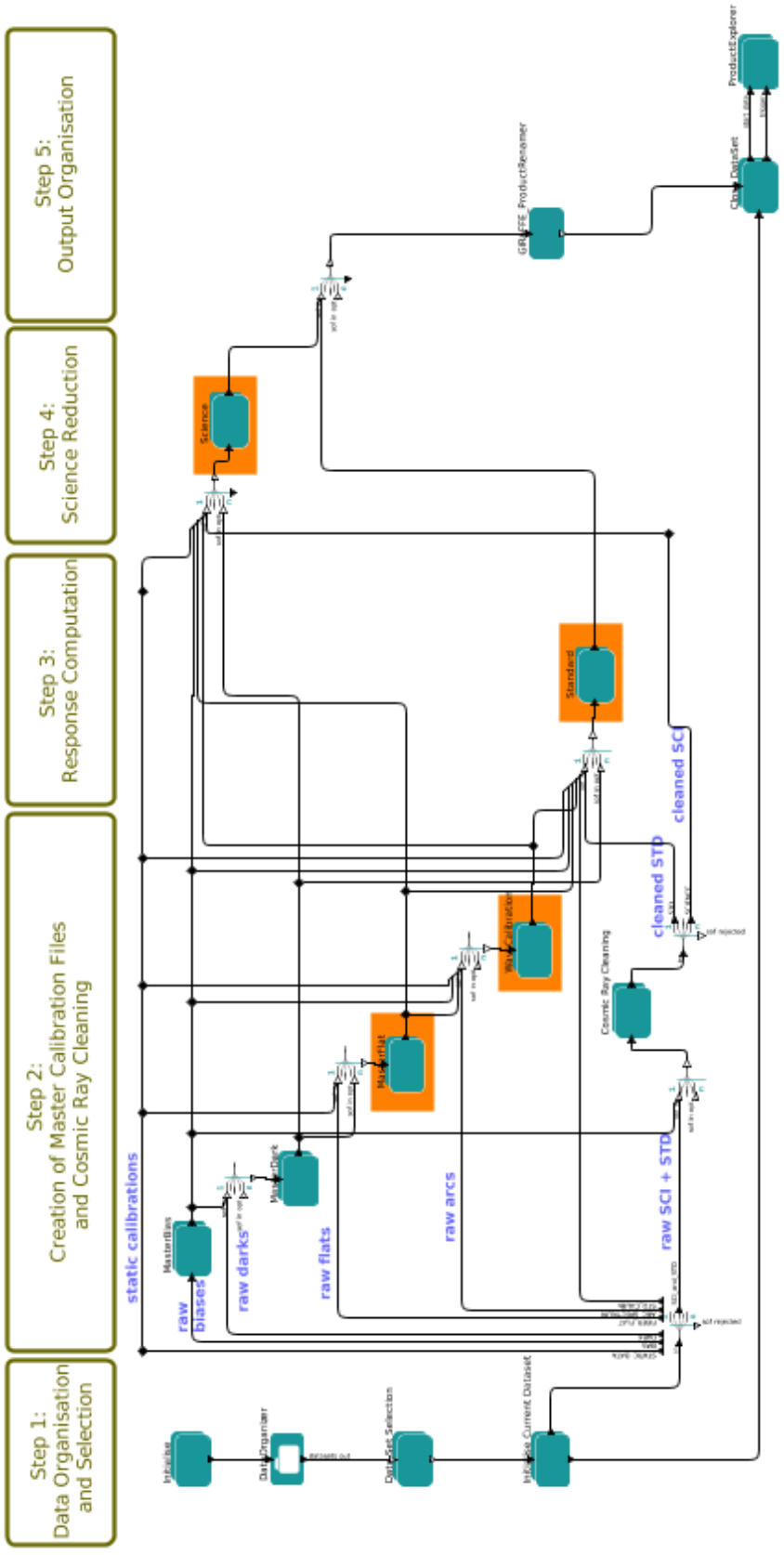

Figure 2.3: The Reflex work-flow pipeline for the GIRAFFE spectrograph. From this the recipe actors, ports of several types, and the recipe director can be seen. The image is the pipeline used in this work.

combination of "actors", composite actors, and ports that link the workflow actors to carry out the reduction pipeline recipe/recipes. The director tells the actors when to act and the actors carry out reduction recipes. These recipes produce and apply master bias, master flat and calibrates the wavelength (arc lamp calibration). The end product is a data cube with a 2-D pixel space and a 3rd spectral dimension. Reflex allows for inspection of the output files at every stage of the reduction process, or the files are available for inspection after reduction is complete in the Reflex output. The workflow area for our particular reduction can be seen in Figure 2.3.

2.2.1 Master Bias

The reduction of raw science data performed with Reflex accounts for the many effects associated with electronic and readout noise on the CCD. One essential effect to account for (and remove from our data) is the bias. There exists a bias on each pixel on the CCD originating from the voltage applied to the CCD to ensure linearity in behaviour, and to avoid negative pixel counts being recorded at readout (Pasquini et al., 2002). The voltage then produces a current that manifests itself as unwanted electron counts registered upon readout of the CCD. To remove the bias several zero second exposures are taken. These zero second exposures contain information on the number of counts associated with the bias. The bias frames are then input to Reflex which makes the master bias with the master bias actor. This process then removes the bias and its associated structure from the raw science frame (Eversberg & Vollmann, 2015).

2.2.2 Master Flats

The next important CCD effects to account for is the variation in sensitivity of each individual pixel in the CCD, therefore the CCD is exposed to a uniformly illuminated source such as the telescope dome or a twilight sky. These flat field

exposures reveal dead pixels on the CCD and the any optical defects such as dust and also reveals pixels with varying sensitivity. Pixels do not all behave in a uniform manner, for different wavelengths each pixel has varying quantum efficiency i.e the ratio of charge carriers (electrons) to photons hitting the detector, therefore flat field images are combined and subtracted, then removed from the science frame in Reflex with the master flats actor.

2.2.3 Dark Frames

Similar to the other calibration data discussed here is dark frames. A dark frame is an exposure taken with the shutter closed for the amount of time comparable to the observation. These frames reveals thermal noise associated with the read out electronics, such as hot pixels or fixed pattern noise. The hot pixels arise when thermal electrons become trapped in the potential of the CCD detector and register counts on the CCD. Thermal electrons and counts from electrons associated with signal are indistinguishable, therefore dark frames (in Reflex) are median combined then subtracted from the science and calibration frames to remove these thermal effects.

2.2.4 Wavelength Calibration

An important part of the reduction of spectroscopic data is the calibration of wavelength or the arc lamp calibration. Without a properly wavelength calibrated spectrum it is not possible to obtain kinematic measurements. The calibration is achieved by exposing the CCD to a light source that has passed through the spectrograph, in our case a Thorium-Argon arc lamp (Pasquini et al., 2002). The Th-Ar spectrum will have strong emission lines in precisely known wavelengths. The emission lines profiles for both arc lamp and observation spectra are then compared. The wavelength and pixel scales are then mapped, therefore the observation and arc

lamp spectra can be correlated. This ensures reliable LOSVD results.

2.3 Sky and Galaxy Subtraction

The next step in the data reduction was to subtract sky emission line and continuum profiles from each wavelength frame in our data cube. These manifest themselves as extra counts on the detector and must be removed if any meaningful science can be extracted from the data. As well as emission from the Earth's atmosphere, most of our cEs lie close to large galaxies and as a result display considerable contaminating light from the host galaxy. The sky subtraction therefore needs to robustly remove both the atmospheric and background galaxy light.

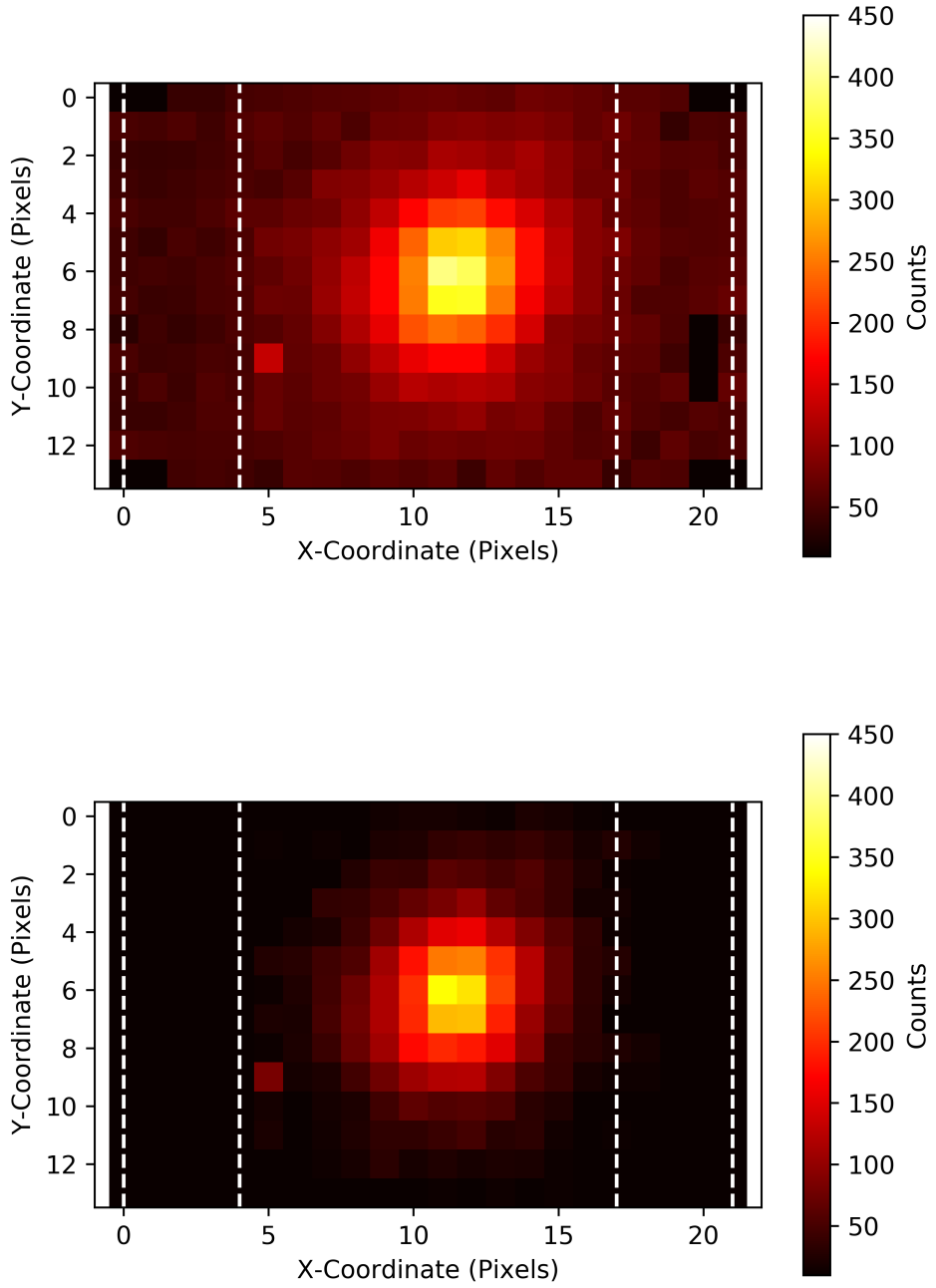

Figure 2.4: A single data cube slice for NGC5846cE pre (top panel) and post sky subtraction (bottom panel). The white dashed lines mark the regions the polynomial fit was applied to. Note the wavelength of these data cube slices are at 8480Å.

Again with the use of Python, the fits files data for our cEs were accessed and for each row of pixels in our 2-D IFUs the count values were plotted. Example plots can be seen in Figures 2.5 and 2.6. From these example plots a noticeable increase in counts can be observed for several rows of pixels (generally in the centre), this is where the the cE is located and where a near horizontal line can be observed is where only the atmospheric and galaxy background is present.

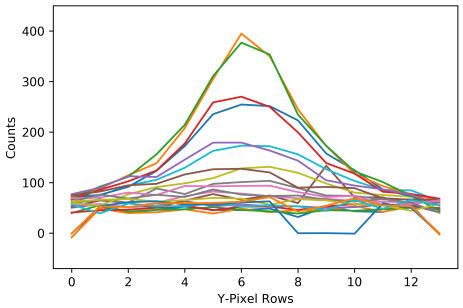

Figure 2.5: Pre-sky subtraction of NGC5846cE. The 14 different colours in the plot represent the 14 Y-pixel rows and the axes are Y-pixel vs counts. A row containing two dead pixels seen as the 2 values of zero is clearly seen.

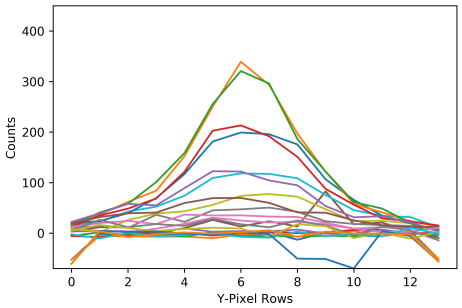

Figure 2.6: Post-sky subtraction of NGC5846cE, by comparing this figure to Figure 2.5 it is clearly seen that the background has been shifted down to the zero line as a result of the subtraction of the fit line.

As can be seen in the plots in Figures 2.5 and 2.6, the pixel rows that represent the outer regions where no cE light should be present have non-zero counts ($\sim$ 50 in this example). This means that our signal from the cEs has contaminating counts and hence must be removed. We removed these extra counts by fitting a polynomial of order 1 i.e. a straight line, to regions either side of the target cEs where little light from the target cE is present (seen in Figures 2.4 in the dashed white marker regions either side of the cE. The pixels 0-4 and 17-21 on the X-axis in this example) and then subtract the fit line to remove the sky, leaving only the signal from our

cEs in the data. The process was then repeated for each row of the IFU, at every wavelength pixel and every exposure. Figure 2.4 shows NGC5846cE pre and post sky subtraction in pixel space, it is obvious by comparing the count values (see the colour bar) that the background has been significantly removed.

The subtracted atmosphere and galaxy background was then saved as a fits file for later use in calculating the SNR in the spatial binning section. With the the sky subtraction performed on each exposure it is necessary to combine each exposure of our cEs together to improve the SNR by a factor of $\sqrt{N}$, where N is the number of exposures. The exposures were combined (summed) with Pyfits in Python. Also at this point before we move onto the next section, the spectral axes of each data cube were collapsed into one dimension i.e the wavelength axis summed, producing a 2-D image of our cEs. The same process was also applied to the data cube containing the background. The spectral axis of the signal and background was collapsed so that the VorBin method can use the resulting images as input for the Voronoi binning step. An example of a summed spectral axis can be seen in Figure 2.7.

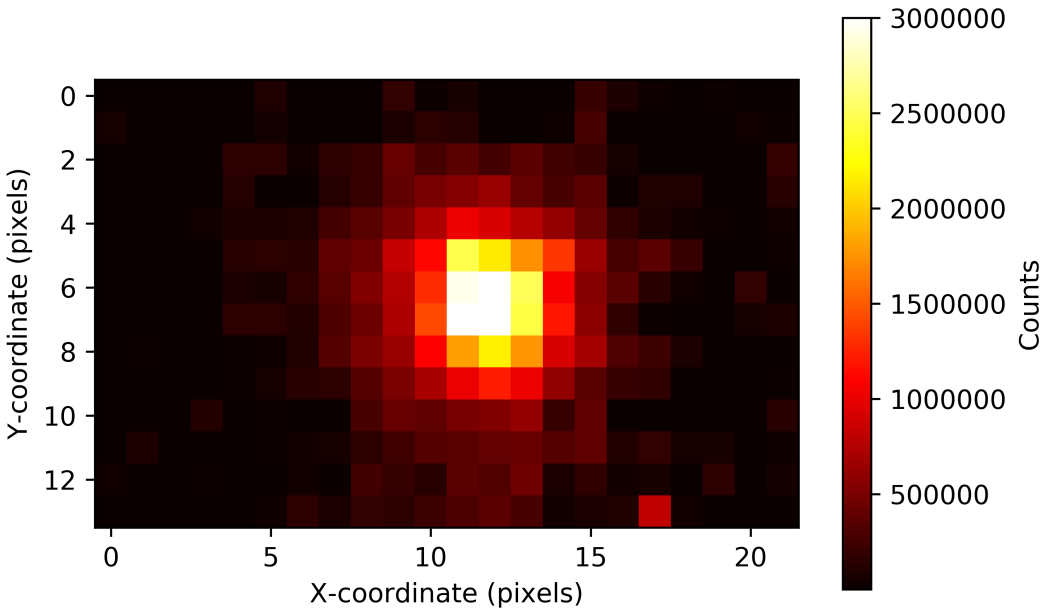

Figure 2.7: An example of the collapsed (summed) wavelength or spectral axis of a data cube for NGC4696cE. VorBin uses the data from such files to perform the binning of spaxels to a constrained minimum SNR in the next section. the colour bar indicates counts.

2.4 VorBin

After the subtraction of sky emission lines and background galaxy light it is crucial to bin the spaxels together to achieve sufficiently high SNR to extract reliable kinematic information while retaining as many spatial bins to be able to extract kinematics from different regions of our cEs. This is implemented with the Voronoi binning method (Cappellari, 2012, 2017a; Cappellari & Copin, 2003). The papers accompanying the Voronoi binning method state that a signal to noise ratio of "50" is needed to extract reliable kinematic measurements. The method uses Voronoi tessellation to bin spaxels with low SNR together to a user defined minimum SNR.

The VorBin method requires 5 input parameters, namely the X and Y coordinates in our 14×22 IFU array and the signal and noise corresponding to each X-Y coordinate and the required minimum SNR for each bin. The method will only bin pixels that are in close proximity so that the binning forms contiguous regions.

The signal and noise was found using data from 2 files, the signal used was the summed wavelength axis data of our now reduced data cube created when the sky and galaxy background were removed in Section 2.3. The noise image was created from the reduced data cube with the addition of the data from the sky and galaxy i.e the noise image is simply $\sqrt{Signal\,image + Background\,image}$. The equation used is found in Equation 2.1 below. The data input to VorBin from the 2 files were converted to the appropriate units of S/N per angstrom, by first dividing each pixel value (i.e. the count values) by the number of wavelength pixels (5980) then by multiplying this number by the ratio of the wavelength scale (1Å/0.2Å= 5) to arrive at the correct units.

$$S/N = \frac{S}{\sqrt{S+B}} \tag{2.1}$$

Where S is our data cube and B is the sky and galaxy background. Other noise sources such as the dark current and readout noise is negligible compared to the signal and background and are therefore omitted for simplicity.

Once these five parameters are input to the method, VorBin then produces three output parameters. These are the X and Y coordinates of each IFU spaxel and for each X-Y coordinate, a specific bin number (BinNum). This BinNum specifies which spaxels are to be summed to produce the combined spectrum i.e adjacent spaxels to be combined into one binned spaxel share the same bin number. The bin maps seen in Figures 2.8 to 2.13 are also produced by VorBin as standard output. These bin maps visually depict which spaxels are to be combined to produce the combined spectra. The top maps in Figures 2.8 to 2.13 of X-Y pixel space shows

colour coded regions of the spectral bins and the bottom map shows the SNR of each bin which is represented with a red dot, the blue line in the bottom map shows the input minimum SNR and the black dots show the SNR of the original pixels. Note: The brighter target cEs with correspondingly originally high signal have many distinct bins (12 and 13), whereas the cEs with an originally low signal have fewer bins (4 to 6) as expected. Only six of the seven original targets are seen in the figures below because our observations of cE ESO1303005 had insufficient S/N for VorBin to produce even a single bin of minimum SNR.

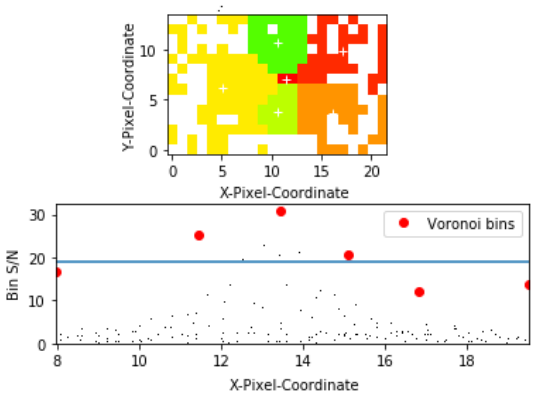

Figure 2.8: The VorBin bin map for the isolated AHcE0. Note how this has half the distinct spatial bins as NGC5846cE.

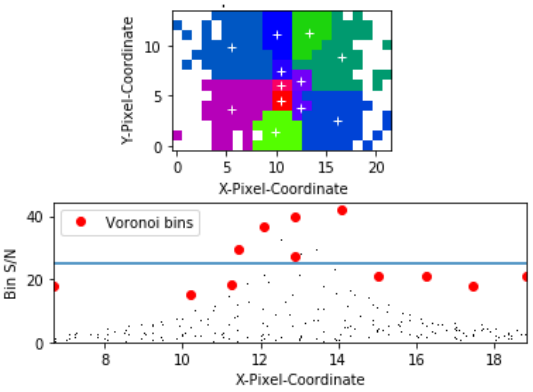

Figure 2.9: The VorBin bin map for NGC5846cE. As can be seen from the bin maps, many spatially distinct bins are available.

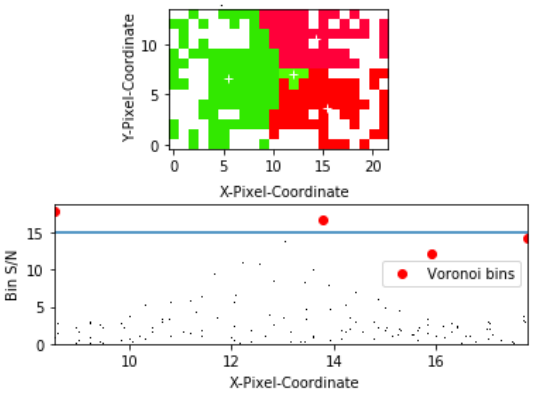

Figure 2.10: The VorBin bin map for Abell400. The white plus symbols represent the light weighted centre of each bin.

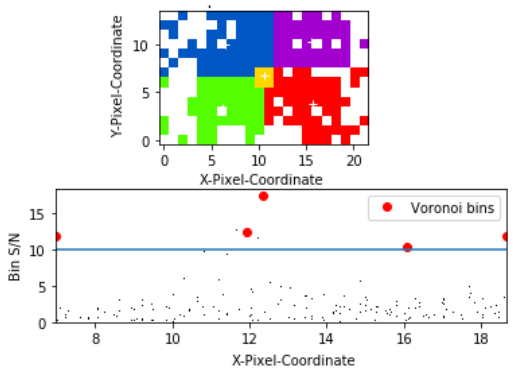

Figure 2.11: The VorBin bin map for Abell496cE. The coloured regions represent the distinct bins.

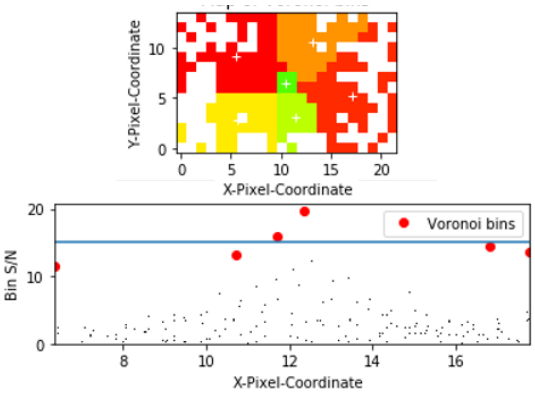

Figure 2.12: The VorBin bin map for NGC3268cE1.

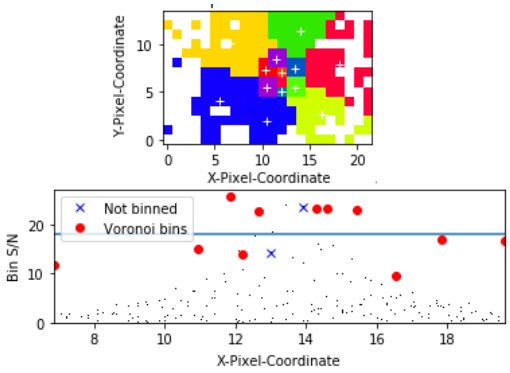

Figure 2.13: The VorBin binmap for NGC4696cE.

Chapter 3

Measurements of Kinematics

If we are to gain insight into the mechanisms that govern galaxy formation, we must first investigate the bulk motion of the stars and gas in galaxies. The motion of the stars in a galaxy can allow us to gain knowledge of the potentials of the gravitational wells of galaxies and therefore helps us understand how they form and evolve in these potentials (Cappellari, 2017a). The central velocity dispersion is especially important as it follows exceptionally tight scaling relations with BH and bulge mass (van den Bosch, 2016). The central velocity dispersion will also be used in deriving estimates of the dynamical masses of our sample cEs.

3.1 Penalized Pixel Fitting (pPXF)

With all the reduction of raw science and binning of spectra complete the next step was to perform a full spectrum fit to our binned 1-D spectra to extract the LOSVD for our remaining cEs. The tool chosen to perform this task was pPXF (Cappellari, 2017b; Cappellari & Emsellem, 2004). pPXF is a powerful tool for extracting stellar and gas kinematics from spectroscopic data. In addition it can also be used to derive star formation histories of galaxies (e.g see Morelli et al., 2013; Norris et al., 2015). however, due to the limitations of the wavelength coverage and SNR constraints we

will focus on kinematic measurements in this thesis.

Since its release in 2004 pPXF has had several upgrades with the latest allowing for a more accurate convolution with the Gauss-Hermite series, this is a series that accounts for the deviations of absorption or emission line profiles from a pure Gaussian and is commonly described by 2 extra moments; the h3 and h4 parameters. Note; the extra moments in the series extend beyond the 3rd and 4th term but these 2 are sufficient for most practical purposes. The h3 parameter describes the anti-symmetric deviation skew i.e the tail of the Gaussian to either the positive or negative direction and the h4 parameter accounts for symmetric deviations from a pure Gaussian; kurtosis. Kurtosis is a measure of how flat topped or peaked the Gaussian is (van der Marel & Franx, 1993). The h3 and h4 parameter deviations from pure Gaussian curves then relate to the group orbital motions of stars contained within a galaxy.

pPXF continues to be used widely for the purposes mentioned above (see e.g Cappellari et al., 2011; Comerón et al., 2015; Taylor et al., 2015). pPXF convolves a set of template spectra with a discretised kernel. This means that if any neighbouring pixel values vary wildly the current pixel is penalised for the discrepancy, which affects the full spectrum fit. During the iterative process of convolution with the discretised kernel, different combinations of template spectra are combined (convolved) with the LOSVD until a good fit to the input spectrum is found. The goodness of fit then indicates how successful the iterative process has been with a reduced χ^2 squared value.

The pPXF method requires several input parameters to be able to perform the full spectrum fit, namely a 1-D spectrum from our cEs, a noise spectrum, a set of template spectra, an initial recessional velocity or red-shift estimate, as well as the instrumental and template spectral resolutions in the wavelength being fit. The main input parameters and how these parameters were obtained will now be discussed in

the following subsections.

3.1.1 Template Stellar Spectra

An integral part of the pPXF method requires the use of a set of template spectra which are combined to fit our observed spectra. Because individual stars in distant external galaxies can not be resolved, the spectra of our cEs consists of a summation of spectra from all of the stars in the galaxy. The template library should then encompass the many spectral types that could be present in the integrated spectrum of the target. The templates used can be synthetic such as the POLLUX database for synthetic stellar spectra (Palacios et al., 2010) or empirical such as The MILES star catalogue (Vazdekis et al., 2010). The synthetic and empirical spectra can consist of simple stellar populations (SSP) of stars all born at the same time and based on models that make assumptions on the star formation rate and the initial mass function. Then many SSPs displaying a range of age and metallicity can be used in conjunction as a set of template spectra.

Due to the lack of available SSPs models in our wavelength range with resolution comparable with our data an empirical template library had to be used. The MILES template library CaT covers the CaII triplet wavelength range of our observations, but only has a resolution of 1.5Å, compared to the 0.85Å for this work. Hence the empirical template spectra used in this work are from the GAIA-ESO survey (Gilmore et al., 2012).

The template stars in this survey were observed using the same instrumental set up as our cE spectra (FLAMES/GIRAFFE) which gives us the same spectral resolution and wavelength range. Our sample of 100 template stars comprise of low mass stars on the main sequence and giants and red giant branch (RGB). The template stars span a range of metallicities, to try and account for the many stellar populations that could be present in our cEs. Because cEs are typically red and

dead (with few, if any young stars), most of the high mass stars will no longer be present in the cEs. This is because high mass stars have relatively short lifetimes and most will have reached the end of their life in supernovae. The intermediate mass stars have moved off the main sequence, leaving low mass and giant branch stars.

The light output of old stellar populations such as our cEs are dominated by RGB stars. Figures 3.1a to 3.1d give an example of the input spectra from low metallicity to high metallicity MS and RGB stars. It is clear from the counts values in these plots that the dominant source of light output comes from the RGB stars. When comparing the low and high metallicity spectra from the plots, it is apparent, that the high metallicity spectrum has many more absorption line profiles. This indicates a greater abundance of heavy elements, hence higher metallicity. Figure 3.2 shows our sample of template stars plotted on a HR diagram expressed in terms of surface gravity and effective temperature, with metallicity indicated with a colour bar. The main sequence and RGB stars are clearly differentiated by the turn off point. he empirical template spectra used in this work are from the GAIA-ESO survey (Gilmore et al., 2012).

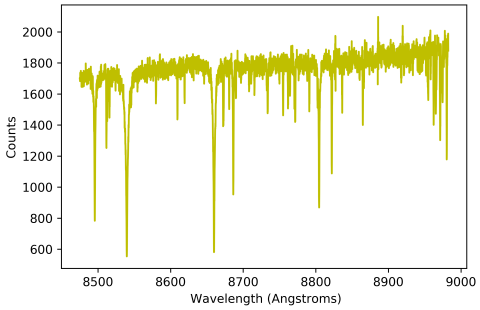

(a) Template spectrum for an intermediate metallicity (-0.47) MS star which represents the low metallicity example in our template sample. The colors of the spectra correspond to the color bar values found in 3.2

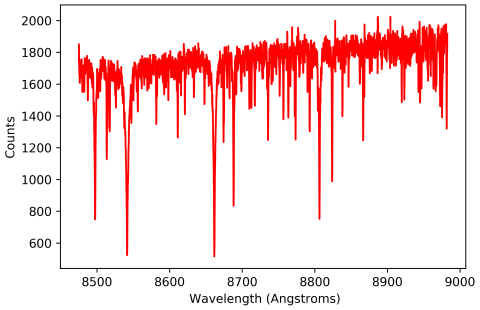

(b) High metallicity (0.42) template spectrum for a MS star. Notice how the number of absorption lines increases for the more metal rich spectra.

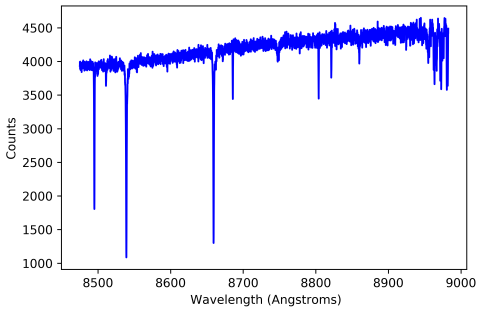

(c) An example of a low metallicity (-2.26) RGB spectrum from our templates. The RGB stars are much brighter than the MS stars, indicated by count value in the plot.

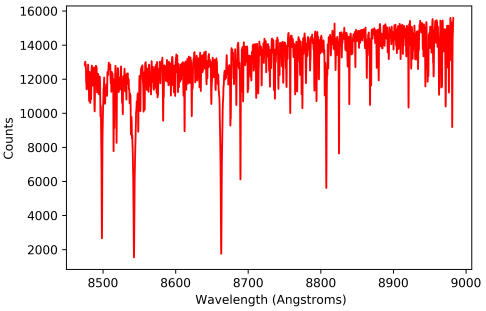

(d) High metallicity (0.32) spectrum for RGB template.

Figure 3.1: The plot show examples of the template spectra for low and high metallicity for main sequence and RGB stars. The colour indicates the metallicity, where blue and yellow represents the low metallicity RGB and MS stars respectively and red indicates metal-rich stars for the RGB and MS, the colours in these figures correspond to the colour bar in Figure 3.2. The CaT is the most prominent i.e strongest absorption feature and visible in all 4 Sub-figures.

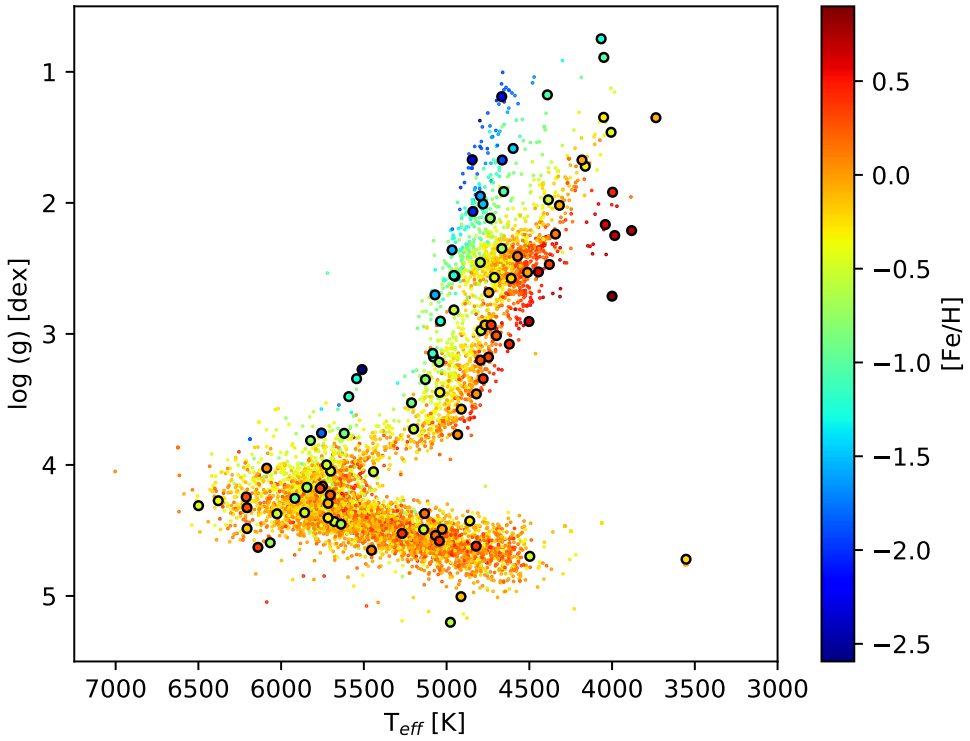

Figure 3.2: A depiction of the template stars to be used with pPXF (highlighted with black circles) The templates consist of low mass main sequence stars and RGB stars. The different colour dots for the stars represent the metallicities of the stars (indicated with a colour bar) where blue is metal-poor and red is metal-rich. The temperatures in this plot range between approximately 6500 and 3500K. Credit:(M.Norris)

3.1.2 Determination of Instrumental Resolution

The instrumental resolution for our observations are found by examining the sky emission line profiles from one of our spectra, therefore we can determine the instrumental resolution by measuring their observed width. This is because these are intrinsically delta functions until they are broadened by the spectrograph, therefore the instrumental resolution was determined by fitting a Gaussian function with Scipy

and Matplotlib in Python, to 12 isolated emission line profiles across our wavelength range (8182-9377Å). The sigma measured from fitting the Gaussian was then converted to Full Width Half Maximum (FWHM) using the equation for the relation between sigma σ and FWHM. FWHM $= 2.355\sigma$, where 2.355 is a conversion factor constant. Figure 3.3 gives an example of the Gaussian fit to a single isolated sky emission line.

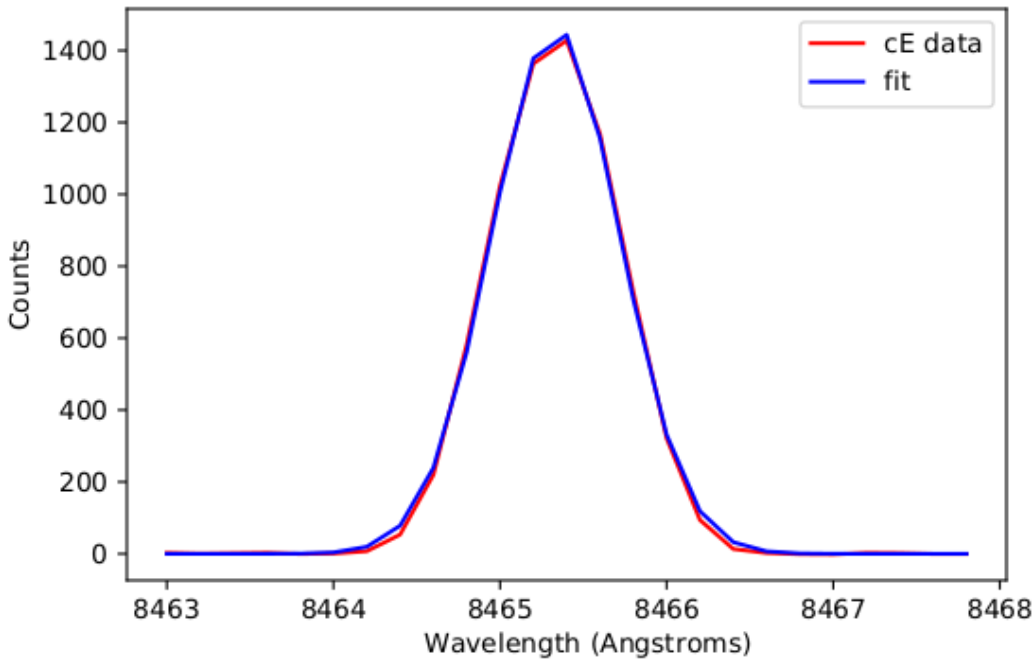

Figure 3.3: An example of the Gaussian fit of an isolated emission line profile. The fit to the emission line was performed with Scipy in Python.

Then a least squares linear fit was applied to the FWHM measurements as a function of wavelength. This was implemented with Python using the LevenbergMarquardt algorithm or LevMar least squares fit of Astropy in Python. The result of this procedure is seen in Figure 3.4. Note: Between the wavelengths of approximately 8500-8750Å and 9100-9350Å no strong isolated sky emission line profiles were available for measurement.

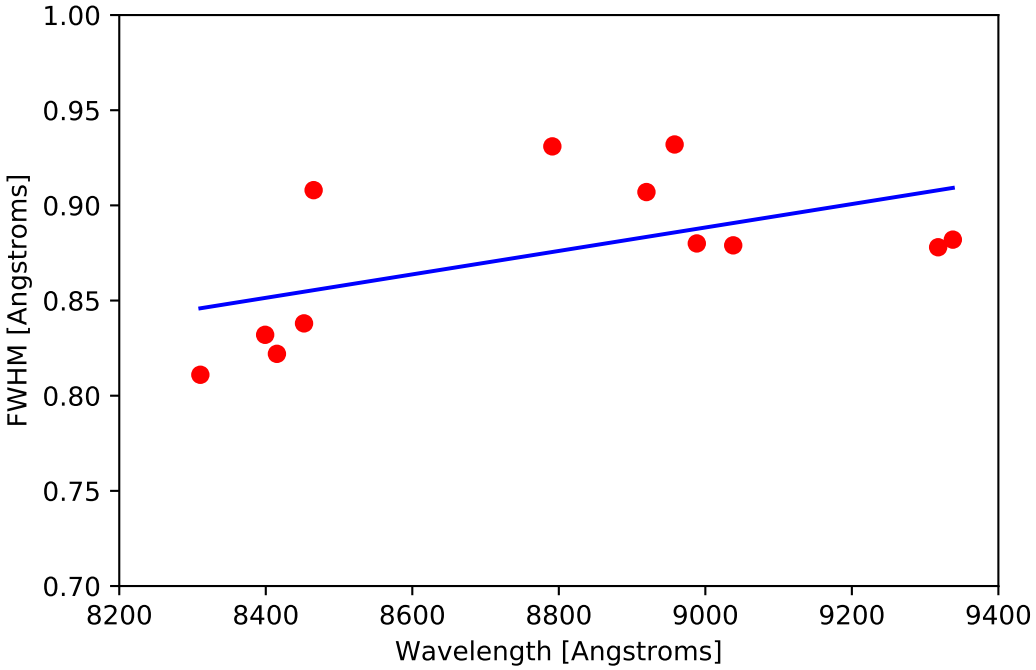

Figure 3.4: The plotted results for the determination of resolution in our wavelength range (8182 to 9377Å). The red circles indicate the FMHM measurements and the least squares fit is indicated with a blue line

From the plot in Figure 3.4 it can be seen that in the wavelength range of the CaII triplet (The three emission lines of the CaII triplet have rest wavelengths at 8498, 8542 and 8662Å respectively), that the FWHM for our observations is $\Delta\lambda \sim 0.85$Å. With this value we can then find the resolution R using the equation below.

$$R = \frac{\lambda}{\Delta\lambda} \tag{3.1}$$

Therefore entering our approximate values for the wavelength range and our measured FWHM, this gives us.

$$R = \frac{8500}{0.85} \sim \ 10,000 \tag{3.2}$$

A result of 10000 ± 171, is a reasonable value compared to the expected value (11000) for the low resolution mode of the ARGUS IFU (Santin et al., 2003). Therefore giving us the resolution in our wavelength range.

At this point we now have all of our main pPXF input parameters, these have been discussed in the previous subsections of this chapter. There are other input parameters to input into pPXF, these include: A noise spectrum, a red shift (or recessional velocity estimate) and the required kinematic moments to fit. The noise estimate can be either a simple file or an empty vector array. The red-shift or recessional velocity estimate was sourced from NASA/IPAC Extra-galactic Database NED `https://ned.ipac.caltech.edu/` these can be found in Table 1.1. Other optional inputs include a cut on the wavelength range. we used the wavelength range of 8480-8800Å, as this wavelength range removed spurious line profiles and noise, from either side of the CaII triplet which sometimes inhibited the fit of our spectra. There is also an option to specify the number of kinematic moments, where 4 would fit moments up to the h4 parameter of the Gauss-Hermite series (mentioned at the beginning of this chapter) and moments set to 2 would perform the fit for only recessional velocity and velocity dispersion. Initially we set moments equal to

4, this however led to severe differences in our recessional velocities compared to the literature values for our cEs, therefore moments were set to 2 in the following analysis.

Chapter 4

Results

In the last chapter we described and discussed how we performed the full spectrum fit for our cEs with the pPXF method. In this chapter we will present the results of the full spectrum fit to our cE data. Out of the remaining six cEs, only four had a sufficient SNR to extract the LOSVD. The four remaining cEs were the well studied NGC5846cE and NGC3268cE1, the isolated AHcE0 and NGC4696cE which-as mentioned before-had no previous central velocity dispersion measurements published. Figure 4.1 shows the full spectrum fit for NGC5846cE performed by pPXF. The results for the recessional velocity V and central velocity dispersion σ_0 can be seen in Table 4.1. The h3 and h4 parameters were not fit as these lead to severe underestimates in the recessional velocity V.

The results were obtained by running pPXF in Python using the options discussed at the end of chapter 3. The CaT region does not have any strong emission lines, pPXF typically has to mask emission lines to be able to recover uncontaminated absorption line kinematics. this is done with the "degree" (additive Legendre polynomial) option in the calling sequence of pPXF. however due to the lack of emission lines in the CaT region, the default mean value of 1 was sufficient. The continuum feature in the spectrum being fit also needs masking. The "mdegree" (the multiplicative Legendre polynomial) option in the pPXF calling is responsible

for this. Again for most spectra the default value was sufficient. To asses whether the the results constituted a good fit, a value of the reduced χ^2 function had values as close to unity as possible and by visual inspection of the fit.

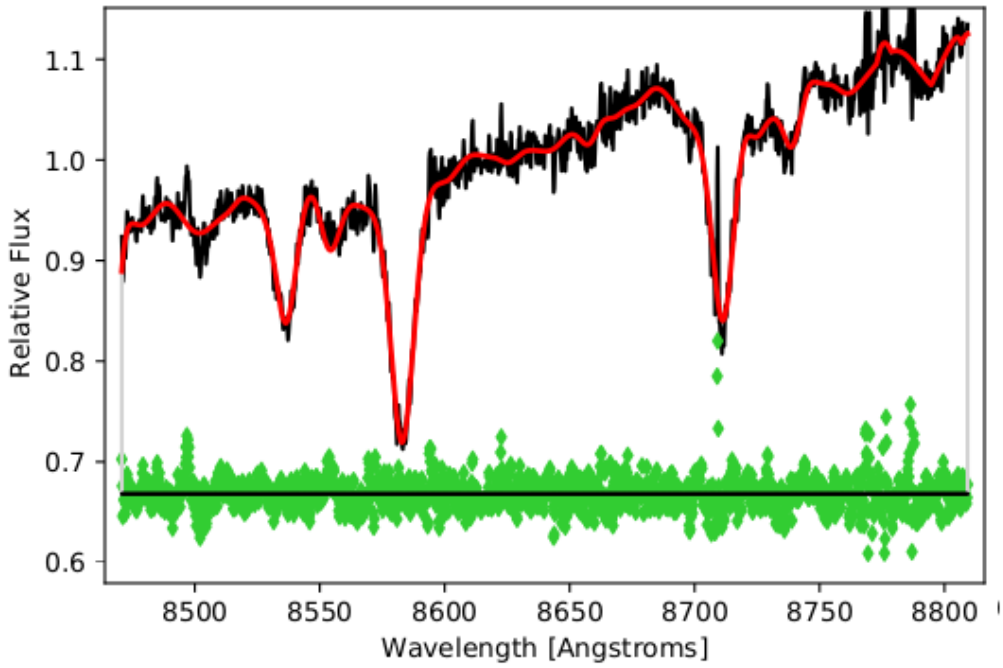

Figure 4.1: An example of a full spectrum fit performed by pPXF. The data marked in black is the spectrum for the central region of NGC5846cE, the red data is the fit, the green data is the residuals, i.e leftover noise.

4.1 Recessional Velocity and σ_0 Measuremnts.

Figure 4.2 is a plot of the measured line of sight velocity or recessional velocity from this work against literature values. The velocities span $21 kms^{-1}$ for NGC5846cE to $77 kms^{-1}$ for AHcE0. Most agree within their mutual 1σ error bars and all agree within 3σ errors, therefore the results agree reasonably well.

Figure 4.3 shows the results for the central velocity dispersion plotted against

Object	V (kms^{-1})	σ_0 (kms^{-1})	V (kms^{-1}) error	σ_0 error (kms^{-1})	χ^2
NGC5846cE	1506	116	3.4	3.2	0.11
NGC3268cE1	2697	42	4.4	3.6	0.83
NGC4696cE	2285	89	10	7.4	0.76
AHcE0	5860	99	7.3	5.4	0.41

Table 4.1: Results for recessional velocity V, the central velocity dispersion (σ_0), the associated errors and the reduced χ^2 goodness of fit measured with the pPXF full spectrum fit for the central spaxel of remaining cEs.

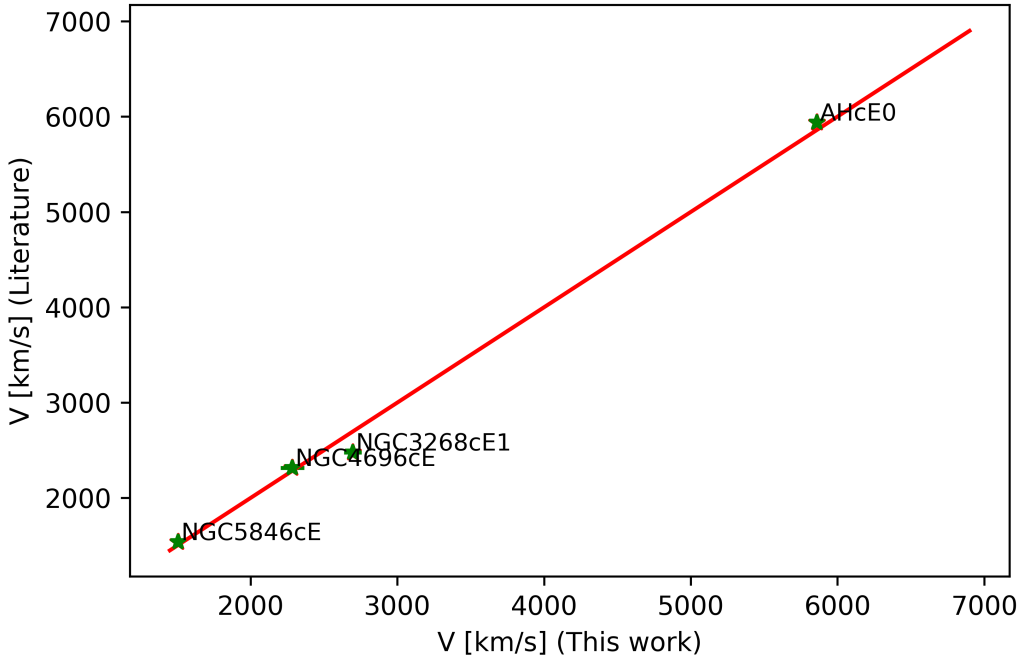

Figure 4.2: Figure for our measured recessional velocity compared to literature values for the 4 remaining cEs. The velocities are consistent within their mutual 3 σ error bars.

the literature values. These results are within 1 sigma errors with literature values except for NGC4696cE, as we have nothing to compare it with (labeled with a red

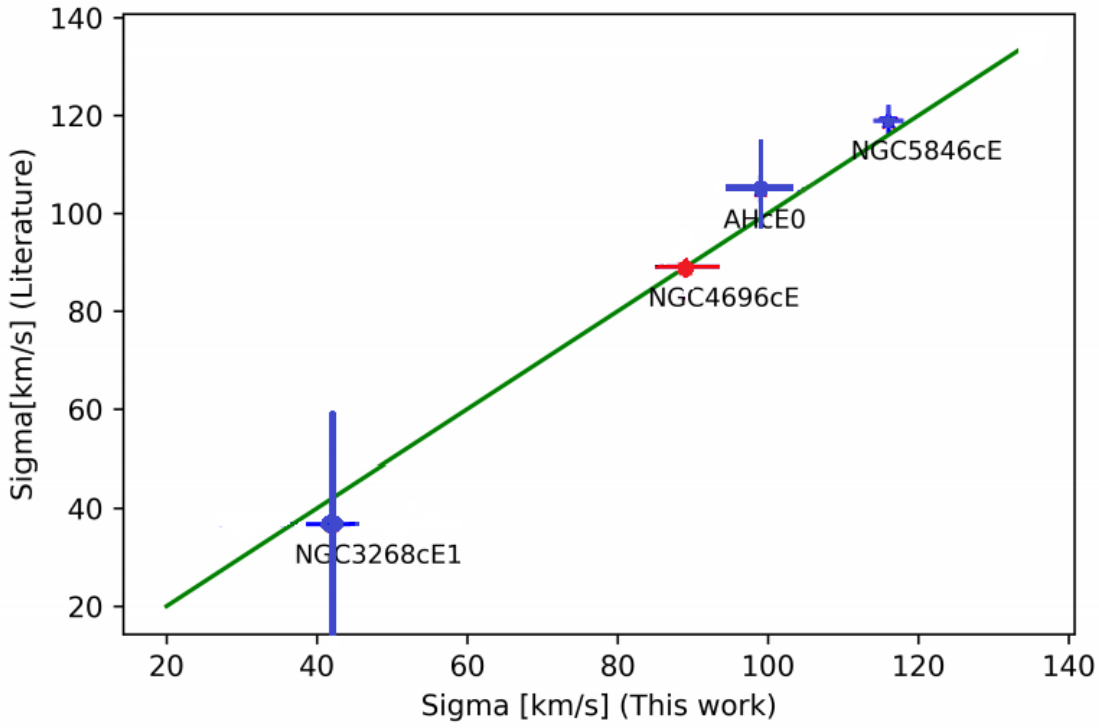

Figure 4.3: Here is a comparison between the results found in this work and results found in the literature for central velocity dispersion. The red marker is NGC4696cE, there are no literature values for this cE, but the values were plotted to show how the measured values for central velocity dispersion σ_0 compared to the other cEs with literature values.

star). We have also significantly reduced the error bars for NGC3268cE1. The reduced χ^2 goodness of fit indicated the full spectrum fit for each cE was performed reasonably well, with $\chi^2 > 1$ indicating an under fit while a $\chi^2 < 1$ indicating an over fit (Bulmer, 2012). For all of the σ_0 measurements having χ^2 ranging from 0.11 to 0.83, therefore the error spectrum is slightly overestimated see Table 4.1.

4.2 Velocity Dispersion Profiles

Figures 4.4 and 4.5 show our derived velocity dispersion at varying radii for two of our cEs. The σ increases at radii approaching the centre (0) from the edges from approximately $39 kms^{-1}$ in the outer regions to $116 kms^{-1}$ in the centre (for NGC5846cE) and from 33 to $89 kms^{-1}$ for NGC4696cE, this is to be expected as the density of stars increases towards the central regions of the cE, although an increase of this magnitude could indicate additional dynamical support from the presence of a SMBH. As we have likely failed to resolve the SMBHs sphere of influence, then the true sigma spike is likely to be even more prominent i.e more peaked when observed with Adaptive Optics (AO).

σ (kms^{-1})	σ error (kms^{-1})	χ^2	Radius (Arcseconds)
37	2.4	1.07	-1.2
96	5.1	0.13	-0.4
116	3.4	0.11	0
110	6.5	0.14	0.4
39	16	1.8	1.2

Table 4.2: Velocity dispersion for NGC5846cE at varying radii. The radii were determined by the pixel scale in our collapsed wavelength images.

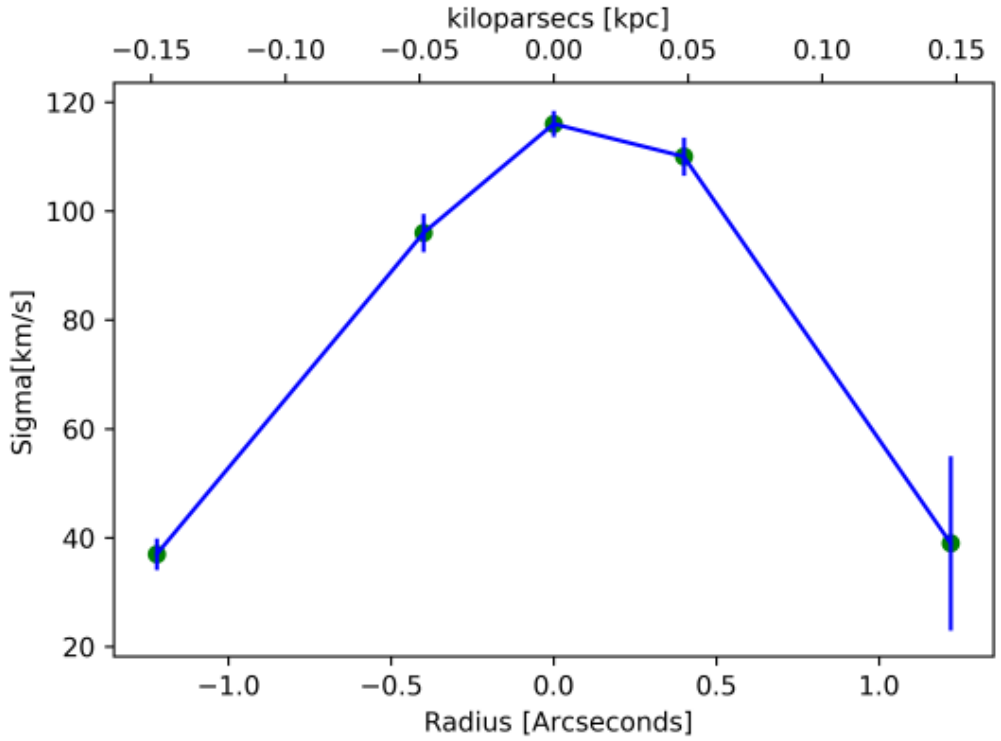

Figure 4.4: σ profile for NGC5846cE. The σ of the cE increases at radii approaching the centre (0).

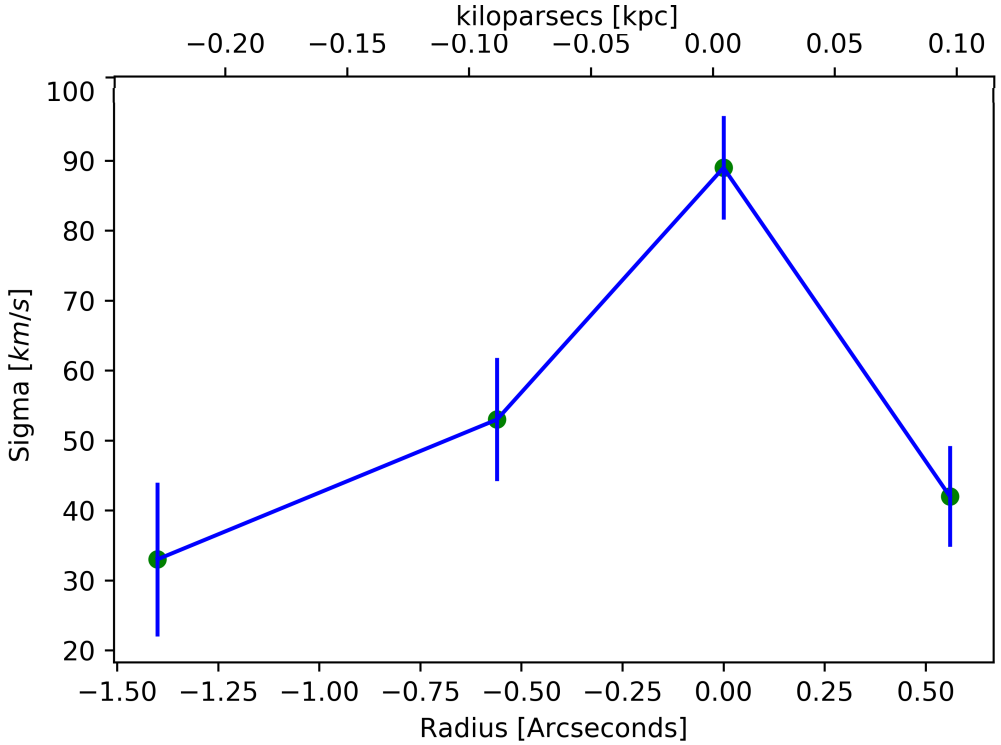

Figure 4.5: σ profile for NGC4696cE. The gravitational influence of a SMBH is most probably the the cause for the increase in sigma values in the central regions ($89 kms^{-}1$)

σ (kms^{-1})	σ error (kms^{-1})	χ^2	Radius (Arcseconds)
33	11	3.2	-1.4
53	8.8	0.43	-0.6
89	7.4	0.76	0
59	8.5	0.59	0.6

Table 4.3: Velocity dispersion (with errors) for NGC4696cE at different radii of the cE. The sharp increase in σ approaching the centre could be due to the presence of a SMBH.

4.3 Dynamical to Stellar Mass Ratios

Now that we have results for the LOSVD (in our case V and σ_0), the next step in the process of obtaining dynamical mass to stellar mass ratio to look for evidence of SMBHs is to use measurements for σ_0 to derive a dynamical mass estimate for our cEs. This was done using Equation 4.1, which is the virial theorem in terms of the total mass of the system and in the form for a none-zero energy bound orbit (Collins, 1978; Forbes et al., 2014). By making the safe assumption that our cEs are virially bound and hence their dynamics are governed by the virial theorem, we adopt the values of 6.5 for the virial coefficient used by (Forbes et al., 2014; Mieske et al., 2013). This coefficient is deemed reasonable for use with our class of CSS because 6.5 corresponds to a Sérsic index of 2. The Sérsic index describes how the surface brightness or light intensity varies with radius for early-type galaxies (Graham & Driver, 2005; Sérsic, 1963). An index of 2 corresponds to a steep decrease in intensity with radius which would be expected for bulges and CSS', where M32 has a Sérsic index of 1.5 (Graham, 2002) therefore an index of 2 is deemed reasonable, however choosing one value for all target cEs could cause errors in results. We will then use the published values for the effective or half light radius R_e taken from NED in Equation (4.1)

$$M_{dyn} = CG^{-1}\sigma_0^2 R_e \tag{4.1}$$

Where M_{dyn} is the dynamical mass, C is the virial coefficient for our class of galaxy 6.5, G is the gravitational constant, σ_0 is the central velocity dispersion and R_e is the effective radius.

Using equation (4.1) we can now arrive at an estimate for the dynamical mass of our cEs. Note: The units used in this equation have to be in SI units, therefore the radius and the velocity dispersion have to be converted to give the results for dynamical mass in terms of kg. Then dividing by solar mass units ($1.989 \times 10^{30} kg$) so the results are in terms of solar mass $M_\odot$ The results can be found in Table **??** below.

Object	$M_{dyn}(10^9 M_\odot)$	$M_{err}(10^9 M_\odot)$	M_* $(10^9 M_\odot)$	R (pc)	$R_{err}(pc)$
NGC5846cE	4.87	0.27	3.24	240	10
NGC4696cE	4.06	0.14	4.47	340	4
NGC3268cE1	0.98	0.70	0.13	299	21
AHcE0	7.39	0.83	4.68	499	10

Table 4.4: Results for Our dynamical mass estimates in solar mass units, their uncertainties, known stellar masses in solar mass units, the effective radii and corresponding errors.

Uncertainties for our estimates for dynamical mass were then propagated with the uncertainties in the cE radii used in equation 4.1. The results can be found in Table 4.5. Note the results in this table were found using equation (4.2).

$$\Delta M_{dyn} = C(\sigma_0 \pm \sigma_0 err)^2 (R_e \pm R_{err})^2 \tag{4.2}$$

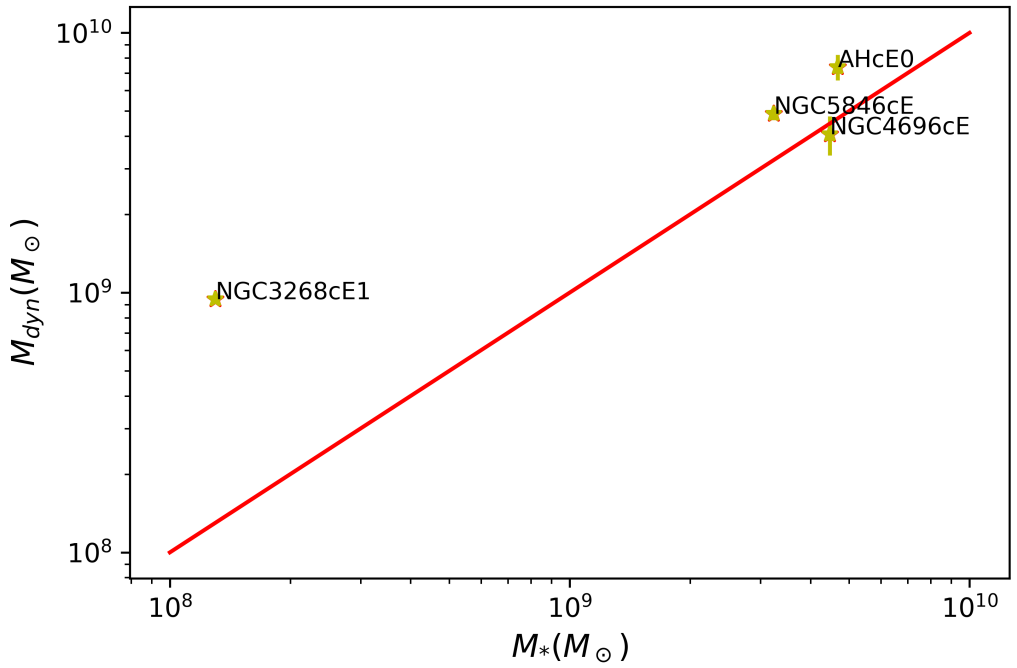

Figure 4.6: Our derived dynamical mass vs stellar mass for four cEs labeled in the Figure. The diagonal red line indicates the unity or 1:1 ratio line. 3 cEs are found display dynamical masses which are inconsistent with their stellar masses, perhaps indicating the presence of an overly massive SMBH.

Object	$\Delta MUpperlimit(10^9 M_\odot)$	$\Delta MLowerlimit(10^9 M_\odot)$
NGC5846cE	0.83	0.57
NGC4696cE	3.04	0.74
NGC3268cE1	3.1	0.39
AHcE0	10.0	6.1

Table 4.5: The uncertainties in our dynamical mass estimates when propagated with the values for effective radii used with equation 4.1.

The Figure 4.6 shows a plot of final results for our dynamical to stellar mass ratios. There are 3 cEs which are above the unity line. These cEs display apparent dynamical masses which are inconsistent with their stellar masses, that is to say the velocity dispersion of stars indicates a deeper gravitational potential than expected. The stellar masses used were those found in the AIMSS project (Forbes et al., 2014; Janz et al., 2016; Norris et al., 2014). Upon inspection of the upper and lower limits of the uncertainties found in Table 4.5, two cEs still have a noticeable inconsistency between stellar and dynamical mass. This most likely is an indication of the presence of a SMBH. If the SMBHs in these cEs are of the order predicted by the literature values for stellar mass and our results for dynamical mass estimates, then the SMBHs are overly massive. The black holes are overly massive for the size of galaxy they reside in and because it is well know, that galaxy mass and black hole mass scale for both early-type and spiral galaxies(Davis et al., 2018), therefore we can reasonably presume that tidal stripping is the causal origin of cE formation.

Chapter 5

Discussion

5.1 Implications Of The Results.

In the last chapter the results were presented. We will now discuss the implications. Out of the original targets only four cE observations had a SNR sufficient to perform the full spectrum fit. The limiting factor with our observations was simply low SNR. For the four cEs with sufficient SNR to arrive at results for the central velocity dispersion, only two cEs had enough spatial bins to be able to examine sigma profiles.

The four cEs (NGC5846cE, NGC4696cE, NGC3268cE1 and AHcE0) we obtained results for central velocity dispersion did have a SNR that was much closer to the required 50, having $\sim$ 40,30,20 and 30 respectively. Therefore the reduced χ^2 goodness of fit in pPXF for the measurements for central velocity dispersion seen in Table 4.1 represented a reasonable fit to the data, hence producing reliable measurements of the LOSVD, with velocity dispersion agreeing within 1 sigma errors and the recessional velocity agreeing within 3 sigma errors of previous literature measurements.

The results for our dynamical mass estimates when plotted against stellar mass values of cEs. The results show a small inconsistency between the dynamical mass estimates of this work and the stellar mass measurements. This hints at the presence

of an overly massive black hole for three out of the four cEs for which measurements were obtained. This is especially true for NGC3268cE1. NGC3268cE1 shows a large inconsistency between stellar mass and dynamical mass estimates. NGC5846cE and AHcE0 have similar σ_0 (116 and $99 kms^{-1}$) and therefore have comparable mass estimates, with both cEs showing a slight hint of possessing overly massive BHs, however not to the extent of NGC3268cE1. NGC4696cE does not show any obvious sign of having a overly massive BH with near 1:1 ratio (within the error bars) of dynamical to stellar mass. It might be the case that the sphere of influence of the central BH-if present-was not resolved and therefore not observed. It could be argued that the velocity dispersion i.e the dispersion about the line of sight velocity of the stars in the cEs could only be influenced in this way is by the presence of a massive body at the centre (a SMBH). In this work we may only conclude that NGC4696cE is made up of mostly stars, if our assumption of no gas or dark matter content present in our cEs is true. It could be said that the sensitivity in choosing the correct virial coefficient and the uncertainties in the measurements, could still yield results near the identity line.

For the two cEs with enough spatial bins to observe velocity dispersion profiles, NGC4696cE shows a sharp increase towards the central regions of the cE (unlike the more shallow profile of NGC5846cE), however this is unlikely to be the true spike in velocity dispersion, therefore improved observations with higher resolution and SNR are required.

5.2 Future Work

As discussed in the last section only four cEs out of our sample had a sufficient SNR to extract kinematic information. As it is deemed essential by Cappellari & Emsellem 2004 to achieve a minimum constant SNR of 50 to extract reliable kinematics and star formation histories using pPXF. The signal to noise for observations

in this work had values between 25 and 30. These were sufficient for single integrated values, but would have to be closer to the required 50 to be able to produce maps of h3 and h4 parameters. The case should be made to re-observe our target cEs with the addition of a larger set of targets for a wider range of environments with the now operational Adaptive Optics (AO) system of the VLT. This would reduce the blurring effect of the atmosphere, therefore allowing observations with improved SNR (closer to the required 50). These improved observations would then allow us to better probe the sphere of influence of any BHs that may be present (e.g see Seth et al. 2014). Observations of a larger sample, from a broader range of environments, with the addition of improved signal to noise would greatly improve our understanding of cE formation. By improving kinematics measurements and obtaining star formation histories with the use of pPXF.

This work could be continued by using the results for recessional velocity for every binned spectra to obtain rotation maps. Rotation maps can then reveal any residual rotation. Information about rotation can be used to determine formation and structural parameters by plotting rotational velocity versus σ (Binney & Tremaine, 2008).

5.3 Conclusion

In this work IFS data for seven cEs were obtained from the 8.2m VLT UT2 using the FLAMES/GIRAFFE spectrograph in ARGUS mode, with the aim of finding evidence for the presence of overly massive SMBHs in the cEs. Evidence of an overly massive SMBH can support a formation scenario in which cEs form via the tidal stripping of a progenitor. The raw scientific data was reduced in several steps. By using EsoReflex to perform the main reduction stage (master flats, bias and dark frames) followed by a subtraction of the sky and galaxy background. The reduced IFS data was then spatially binned to a constrained minimum SNR with the Voronoi

binning method VorBin. A full spectrum fit to the spatially binned spectra were performed using the penalized pixel fitting method pPXF to extract the LOSVD, in this case the line of sight velocity and velocity dispersion.

The central velocity dispersion for four remaining cEs were obtained. By using the virial theorem with literature values for effective radius and the measured central velocity dispersion, dynamical mass estimates of the cEs were obtained. Then by using literature values for the stellar masses, the dynamical to stellar mass ratios revealed that three out of the four cEs showed evidence for the presence of an overly massive SMBH which favors the tidal stripping scenario, however further observations with improved signal to noise and resolution are needed to strengthen this conclusion. The case should be made to follow up observation with the now operational AO system of the VLT. The AO system could then be used to obtain observations with a higher SNR, to resolve the BHs sphere of influence. To attempt to observe a true spike in the σ profiles, hence the true central velocity dispersion. This could then be used to accurately determine the true BH mass, and hence through the BH-bulge mass relation, determine the mass of the progenitor.

Bibliography

Bacon, R., Adam, G., Baranne, A., et al. 1995, The Astrophysical Journal, 113, 347

Binney, J. & Tremaine, S. 2008, Galactic Dynamics: Second Edition

Bulmer, M. 2012, Principles of Statistics, Dover Books on Mathematics (Dover Publications)

Bundy, K., Bershady, M. A., Law, D. R., et al. 2015, The Astrophysical Journal, 798, 7

Cappellari, M. 2012, pPXF: Penalized Pixel-Fitting stellar kinematics extraction, Astrophysics Source Code Library

Cappellari, M. 2017a, Monthly Notices of The Royal Astronomical Society, 466, 798

Cappellari, M. 2017b, Monthly Notices of The Royal Astronomical Society, 466, 798

Cappellari, M. & Copin, Y. 2003, Monthly Notices of The Astronomical Society, 342, 345

Cappellari, M. & Emsellem, E. 2004, Publications of the Astronomical Society of the Pacific, 116, 138

Cappellari, M., Emsellem, E., Krajnović, D., et al. 2011, , 413, 813

Chilingarian, I., Cayatte, V., Chemin, L., & Durret, F. 2008, in IAU Symposium, Vol. 245, Formation and Evolution of Galaxy Bulges, ed. M. Bureau, E. Athanassoula, & B. Barbuy, 75–76

Chilingarian, I., Cayatte, V., Revaz, Y., et al. 2009, Science, 326, 1379

Chilingarian, I. V. & Bergond, G. 2010, Monthly Notices of The Royal Astronomical society, 405, L11

Collins, II, G. W. 1978, The virial theorem in stellar astrophysics

Comerón, S., Salo, H., Janz, J., Laurikainen, E., & Yoachim, P. 2015, Astronomy Astrophysics, 584, A34

Courtes, G. 1982, in Astrophysics and Space Science Library, Vol. 92, IAU Colloq. 67: Instrumentation for Astronomy with Large Optical Telescopes, ed. C. M. Humphries, 123

Davis, B. L., Graham, A. W., & Cameron, E. 2018, The Astrophysical Journal, 869, 113

Dekker, H., D'Odorico, S., Kaufer, A., Delabre, B., & Kotzlowski, H. 2000, in , Vol. 4008, Optical and IR Telescope Instrumentation and Detectors, ed. M. Iye & A. F. Moorwood, 534–545

Du, M., Debattista, V. P., Ho, L. C., et al. 2018, arXiv e-prints

Eisenhauer, F., Abuter, R., Bickert, K., et al. 2003, in , Vol. 4841, Instrument Design and Performance for Optical/Infrared Ground-based Telescopes, ed. M. Iye & A. F. M. Moorwood, 1548–1561

Eversberg, T. & Vollmann, K. 2015, Some Remarks on CCD Detectors (Berlin, Heidelberg: Springer Berlin Heidelberg), 387–409

Ferré-Mateu, A., Forbes, D. A., Romanowsky, A. J., Janz, J., & Dixon, C. 2018, Monthly Notices of The Royal Astronomical Society, 473, 1819

Forbes, D. A., Norris, M. A., Strader, J., et al. 2014, Monthly Notices of the Royal Astronomical Society, 444, 2993

Freudling, W., Romaniello, M., Bramich, D. M., et al. 2013, Astronomy Astrophysics, 559, A96

Gilmore, G., Randich, S., Asplund, M., et al. 2012, The Messenger, 147, 25

Graham, A. W. 2002, The Astrophysical Journal, 568, L13

Graham, A. W. & Driver, S. P. 2005, Publications of the Astronomical Society of Australia, 22, 118

Häring, N. & Rix, H.-W. 2004, The Astrophysical Journall, 604, L89

Huxor, A. P., Phillipps, S., & Price, J. 2013, Monthly Notices of The Astronomical Society, 430, 1956

Huxor, A. P., Phillipps, S., Price, J., & Harniman, R. 2011, in EAS Publications Series, Vol. 48, EAS Publications Series, ed. M. Koleva, P. Prugniel, & I. Vauglin, 257–258

Infante, L., Mieske, S., & Hilker, M. 2003, Astrophysics and Space Science, 285, 87

Janz, J., Norris, M. A., Forbes, D. A., et al. 2016, Monthly Notices of The Royal Astronomical Society, 456, 617

Kormendy, J., Fisher, D. B., Cornell, M. E., & Bender, R. 2009, Astrophysical journal, 182, 216

Martinović, N. & Micic, M. 2017, Monthly Notices of the Royal Astronomical Society, 470, 4015

Mieske, S., Frank, M. J., Baumgardt, H., et al. 2013, Astronomy Astrophysics, 558, A14

Monachesi, A., Trager, S. C., Lauer, T. R., et al. 2012, Astrophysical journal, 745, 97

Morelli, L., Calvi, V., Masetti, N., et al. 2013, Astronomy Astrophysics, 556, A135

Norris, M. A., Escudero, C. G., Faifer, F. R., et al. 2015, Mothnly Notices of The Royal Astronomical Society, 451, 3615

Norris, M. A., Kannappan, S. J., Forbes, D. A., et al. 2014, Monthly Notices of The Royal Astronomical Society, 443, 1151

Palacios, A., Gebran, M., Josselin, E., et al. 2010, Astronomy and Astrophysics, 516, A13

Pasquini, L., Avila, G., Blecha, A., et al. 2002, The Messenger, 110, 1

Santin, P., Di Marcantonio, P., Popovic, D., & Pozna, E. 2003, Memorie della Societa Astronomica Italiana Supplementi, 3, 304

Sérsic, J. L. 1963, Boletin de la Asociacion Argentina de Astronomia La Plata Argentina, 6, 41

Seth, A. C., van den Bosch, R., Mieske, S., et al. 2014, Nature, 513, 398400

Taylor, M. A., Puzia, T. H., Gomez, M., & Woodley, K. A. 2015, The Astrophysical journal, 805, 65

van den Bosch, R. C. E. 2016, The Astrophysical Journal, 831, 134

van der Marel, R. P. & Franx, M. 1993, The Astrophysical Journal, 407, 525

van Dokkum, P. G. 2001, Publications of the Astronomical Society of the Pacific, 113, 1420

Vazdekis, A., Sánchez-Blázquez, P., Falcón-Barroso, J., et al. 2010, Monthly Notices of The Astronomical Society, 404, 1639

Vivès, S. & Prieto, E. 2005, submitted to Optical Engineering.

Wirth, A. & Gallagher, III, J. S. 1984, Astrophysical journal, 282, 85

Yıldırım, A., van den Bosch, R. C. E., van de Ven, G., et al. 2017, Monthly Notices of The Royal Astronomical Society, 468, 4216

noneyear year